Complete neuroanatomy and sensor maps of Odonata wings for fly-by-feel flight control

Joseph Fabian[1,2]*, Igor Siwanowicz[3]*, Myriam Uhrhan[1], Masateru Maeda[4], Richard J Bomphrey[4] and Huai-Ti Lin[1]**

1. Imperial College London
2. Flinders University
3. HHMI Janelia Research Campus
4. Royal Veterinary College

*equal contribution authors
** corresponding author

Summary

"Fly-by-feel" describes how flying animals capture aerodynamic information via their wings' sensory system to implement or enhance flight control. Traditional studies on animal flight emphasized controlling body stability via visual or inertial sensory inputs. In line with this, it has been demonstrated that wing sensory systems can provide inertial state estimation for the body. What about the state estimation of the wings themselves? Little is known about how flying animals utilize their wing sensory systems to monitor the dynamic state of their highly deformable wings. This study is a step toward a comprehensive investigation of how a flying animal senses aerodynamic and aeroelastic features of the wings relevant to flight control.

Odonates: dragonflies and damselflies, are a great model for this because they have excellent flight performance and their wing structure has been extensively studied. Here, we developed a strategy to map the entire sensory system of Odonata wings via confocal microscopy. The result is the first complete map of a flying animal's wing sensory system, including both the external sensor morphologies and internal neuroanatomy. This complete search revealed over 750 sensors on each wing for one of the smallest dragonfly species and roughly half for a comparable size damselfly. We found over eight morphological classes of sensors, most of which resembled mechanosensors. Most sensors were innervated by a single neuron with an innervation pattern consistent with minimising wiring length. We further mapped the major veins of 13 Odonate species across 10 families and identified consistent sensor distribution patterns, with sensor count scaling with wing length. To explain the strain sensor density distribution along the major veins, we constructed a high-fidelity finite element model of a dragonfly wing based on micro-CT data. This flapping wing model revealed dynamic strain fields and suggested how increasing sensor count could allow encoding of different wing states. Taken together, the Odonate wing sensory system is well-equipped to implement sophisticated fly-by-feel flight control.

Introduction

Animal locomotion relies on local sensory feedback, where body movements and mechanical forces are monitored and used to inform motor commands. In terrestrial animals, proprioceptors in joints and muscles establish the timing and magnitude of important mechanical events during walking. The wings of flying animals experience inertial and aerodynamic ('aeroelastic') loads, airflow stagnation and separation, and non-linear phenomena of vortex growth and shedding, generated during gliding and flapping flight (Bomphrey and Godoy-Diana, 2018; Dickson et al. 2006; Combes and Daniel 2003). The current literature on mechanical feedback during flight mostly consists of isolated reports of specific sensor types, often accompanied by proposals of their functional significance for flight control. The feather follicles of birds possess mechanosensors sensitive to feather motion under aeroelastic forces (Brown and Fedde, 1993; Carruthers et al., 2007), while the wings of bats and moths are populated with mechanosensors which are known to contribute to flight control and body stabilisation

(Sterbing-D'Angelo et al., 2011; Dickerson et al., 2014). However, complete descriptions of the sensor arrangement on the wings of a flying animal have been elusive. In reality, wings express a diverse array of sensor types each capturing unique and localised mechanical forces depending on their structure and position. As with sensory receptors in other organs, such as the eye, it is likely that arrays of receptors function in concert, each contributing a piece to a larger, time-dependent, sensory mosaic. Therefore, to understand the function of sensory feedback during flight we must first determine a comprehensive map of mechanosensors on wings.

Flying insects are a useful model for studying mechanosensory feedback during flight due to their small size, simple nervous system, and exquisite flight behaviour. Flapping flight relies on the phasic generation of precise aerodynamic forces through coordinated movements of multiple wings. Dragonfly flight is especially interesting due to their four independently controlled wings, each with adjustable amplitude, frequency, and angle of attack (Ruppel, 1989; Thomas et al., 2004). This enables a large wing state-space, each with unique, and time-dependent, aerodynamic and inertial characteristics. Dragonflies can fly by synchronised flapping of all four wings, out-of-phase flapping of forewing and hindwing, isolated flapping of the forewings only, gliding with the wings in a more-or-less stationary position, and even in mechanically linked tandem flights with a mating partner. Furthermore, the ancestor of Odonates represents the earliest flying animal on earth (Misof et al., 2014). From a practical perspective, dragonfly wings have transparent, scaleless membranes, and are relatively large, facilitating e the mapping of external and internal anatomy.

The concept of sensory feedback from insect wings has received attention from neuroscientists and engineers since the 1960's, following the discovery of neurons sensitive to wing twist in locusts (Gettrup, 1966; Wilson, 1961). However, at that time it was difficult to produce a detailed map of sensors or to characterise wing deformation with high fidelity. Further electrophysiological studies described the afferent signals of campaniform sensilla (CS) in the wing in flies (Dickinson 1990). These strain sensors tend to fire a single action potential per wing stroke, so they cannot provide continuous, analogue strain estimation. Instead, strain is believed to be encoded predominantly through spike timing, which varies with the strain spike threshold, and the magnitude of local strain (Dickerson et al., 2014; Yarger and Fox, 2018). Unlike other insects, flies (and Strepsiptera) have a specialized club-like structure called halteres, derived from a reduced hindwing. Instead of a direct role in force production during flight, the halteres express strain sensors which allow indirect estimation of the insect's body rotation (Pringle, 1948). All flapping insect wings experience similar Coriolis forces due to body rotation, and more recent work has proposed that strain sensor arrays on wings may also function as an inertial sensor, much like the halteres (Pratt et al., 2017; Jankauski et al., 2017). However, the wing-mounted sensors are well-placed to monitor the instantaneous aeroelastic loading conditions and flow velocities of the wings themselves. This line of investigation is far less well developed and can have extensive potential impact in bioinspired flight control.

Here we provide the most complete description of the mechanosensory system of an animal wing to date. Specifically, we identify the patterns of neural innervation, the locations of several discrete sensor types, and the patterns of mechanical deformation likely to be experienced by one class of sensors using a custom high-fidelity finite element model of a dragonfly wing. In doing so, we shed light on how the nervous systems could be encoding and represent aeroelasticity.

Results and Discussion

Odonata wing veins house an extensive network of sensory neurons

To visualise the neuronal innervation within Odonate wings, we developed a new approach for penetrating the wing cuticle and labelling the complete collection of wing neurons (see Methods). For comparison, we visualise wings from a small dragonfly species *Perithemis tenera* and a similarly sized damselfly *Argia apicalis*. We identify axons of sensory neurons in all major longitudinal veins. Some of these axons run the entire wing length, making them among the longest neurons in the dragonfly. Axons terminate with a soma which is almost always located directly under an external cuticular

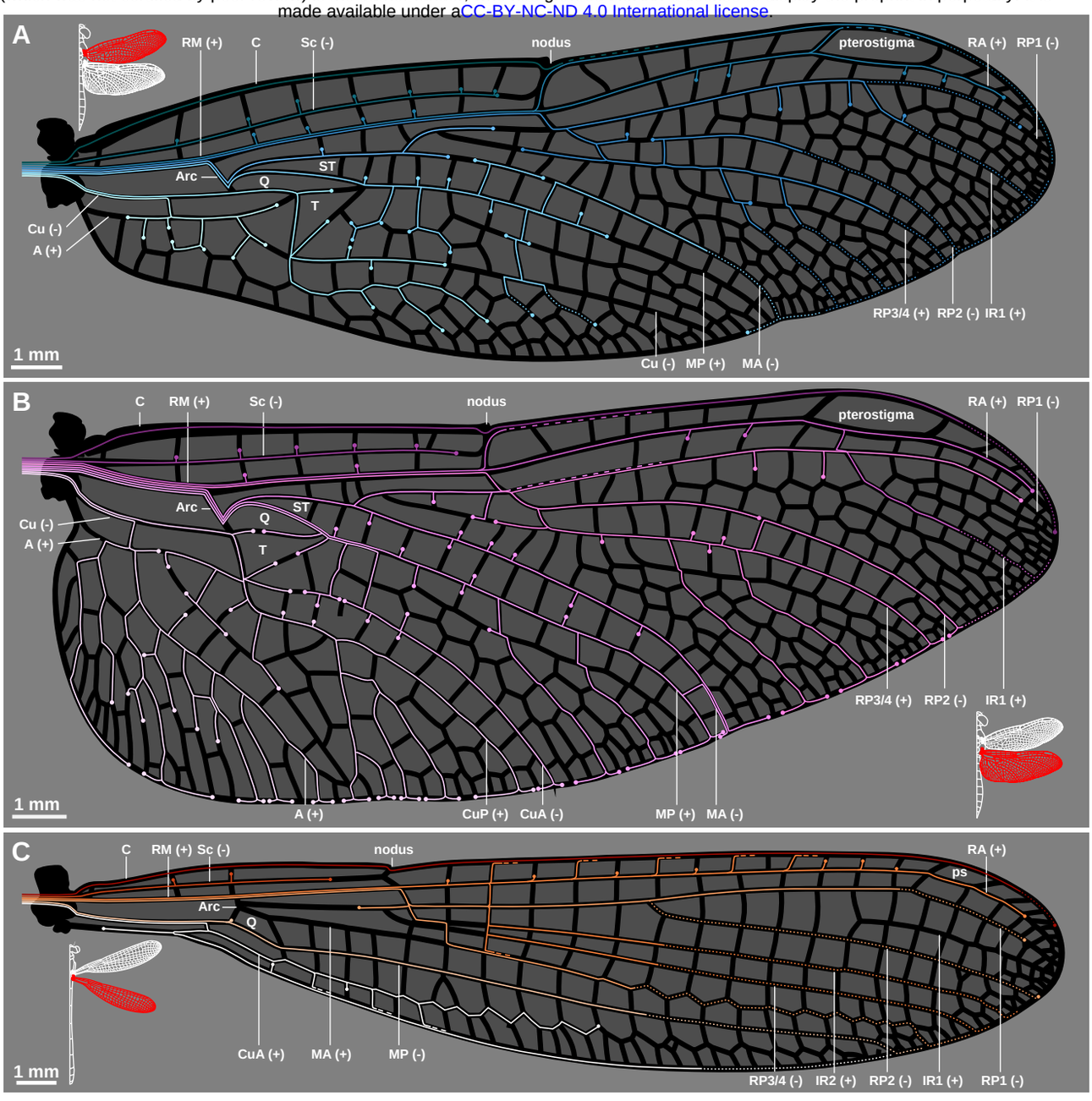

Figure 1: The axon routing pattern of selected Odonates.
Neuronal innervation diagram of a male Eastern Amberwing dragonfly (Perithemis tenera) forewing (A), hindwing (B) and a male Blue Fronted Dancer damselfly (Argia apicalis) hindwing (C). A dedicated afference wing nerve branches out into different veins from the wing base. The color tones of axonal tracks were chosen arbitrarily to aid readability. They do not imply hierarchy or relationships of the tracks. Dots indicate the ends of axonal track; dashed lines denote merging tracks; dotted lines represent tracks that were interpolated from incomplete back-fill images and mechanosensors found on the veins. Major veins and structural elements of the wings are labeled following the system of Riek and Kukalova-Peck (1984) and Bechly (1995): C – costa; Sc – subcostal; RM – radius/media; Cu – cubitus; A – anal; Arc – arculus; T - tringle; ST – supratriangle; Q - quadrilateral. The corrugations of the wings/topology of veins are represented by "+" for "ridges" (dorsally convex) and "-" for "valleys" (dorsally concave).

structure. Each neuron follows a direct, efficient path from the wing hinge to soma (Figure 1A,B), with some minor variation between individuals. Unlike the leading edge and the longitudinal veins, the trailing edge has no dedicated axon tract. Instead, it is innervated locally by extensions of the closest longitudinal vein tracts. This could reduce total axon length, since the medial region of the trailing edge follows a curved and less direct path compared to other major veins. This arrangement will also minimize the impact of typical wing damage, which is almost exclusively found on the trailing edges for dragonflies (Rajabi et al., 2017). If trailing edge sensory neurons were routed along the trailing edge vein, even a small local break would likely eliminate the function of all sensors distal to the damage.

In contrast to the dragonfly, the venation pattern of damselfly wings consists of mostly well aligned rectangular cells, resembling an aerial view of a modern city grid. The innervation pattern of damselfly wings is similar to that of dragonflies, with some exceptions (Figure 1C). Unlike the dragonfly wing, the trailing edge of the damselfly wing is innervated directly, with a tract of axons running along the length of the trailing edge. Due to the wing shape, axons can pass through the damselfly trailing edge without any additional axon length cost. All wing neurons can be traced back to the meso- and meta-thoracic ganglia via anterior and posterior wing nerves originating from the wing base. These two nerves converge before merging into the first nerve bifurcation of each ganglion (Kondo, 1978; Simmons 1977). There is no evidence of interconnection between the neurons within the wing and the cell body counts exceed 750 for each dragonfly wing and 350 for each damselfly wing we mapped. Together it suggests a high maximum influx of raw sensory signals traveling back to the ganglia. The diversity and distribution of these wing sensors will be the focus of the following sections.

The morphologies of wing sensors

Dragonfly wings are extensively innervated by sensory neurons, but what external cuticular structures are these neurons innervating? Odonate wing membranes are smooth, but their veins are covered in an array of microscopic structures with a variety of roles (Rajabi et al., 2011; Gao et al., 2013). Some microstructures resemble sensors, but are not innervated. At high magnifications, we could trace individual axons branching from the primary bundle near the wing hinge and terminating at cell bodies. These cell bodies send thin dendrites towards the cuticular surface. Autofluorescence of this cuticular surface highlights a variety of structures. Based on our current understanding of insect wing sensors, we classified the wing sensory structures into eight main classes: wing margin bristle-bump complexes (Figure 2A,B,C); bristle-bump complexes (Figure 2D); isolated bristles of varying length (Figure 2E, F); campaniform with an associated structure (Figure 2G,H,J); isolated campaniform (Figure 2I,K,L); campaniform sensilla fields (Figure 2M,N); hair plates (Figure 2N,O); and multipolar cells (Figure 2P,Q,R).

The costa vein (leading edge) and trailing edge of the wing are covered in regularly spaced sensory bristles (approximately 30 µm long), placed along the regular serrated cuticle segments (Figure 2A-C). Similar bristles have been found on the wing margin of moths, sensitive to directional vibratory airflow (Ai et al., 2010), and in drosophila, where manual stimulation triggers a defensive leg kicking response (Li et al., 2016). In the dragonfly, each bristle has a neuronal dendrite at its base, and in up to 25% of cases a second sensory neuron sends its dendrite through the shaft of the bristle to its tip. These are the only wing sensors that are innervated by more than one neuron. We suspect double innervated bristles might serve as a chemosensor as seen in flies (Houot et al., 2017) as well as a mechanosensor. Dragonflies are often considered anosmic due to their minuscule antennal lobes (Fabian et al., 2020), but there is some behavioural evidence suggesting odours are used to locate prey (Piersanti et al., 2014). Dragonflies are not able to groom their wings like a fly, but we do not exclude the potential tactile functions for wing margin bristles. Other longitudinal veins have isolated bristles with lengths ranging from 20 µm (Figure 2D) to more than 200 µm (Figure 2E), each innervated by a single sensory neuron at their base. They resemble the trichoid sensilla found in locusts that detect wind direction and elicit compensatory reflexes (Camhi, 1969; Bacon and Tyrer, 1979; Pfluger and Wolf, 2013; McCorkell, 2016).

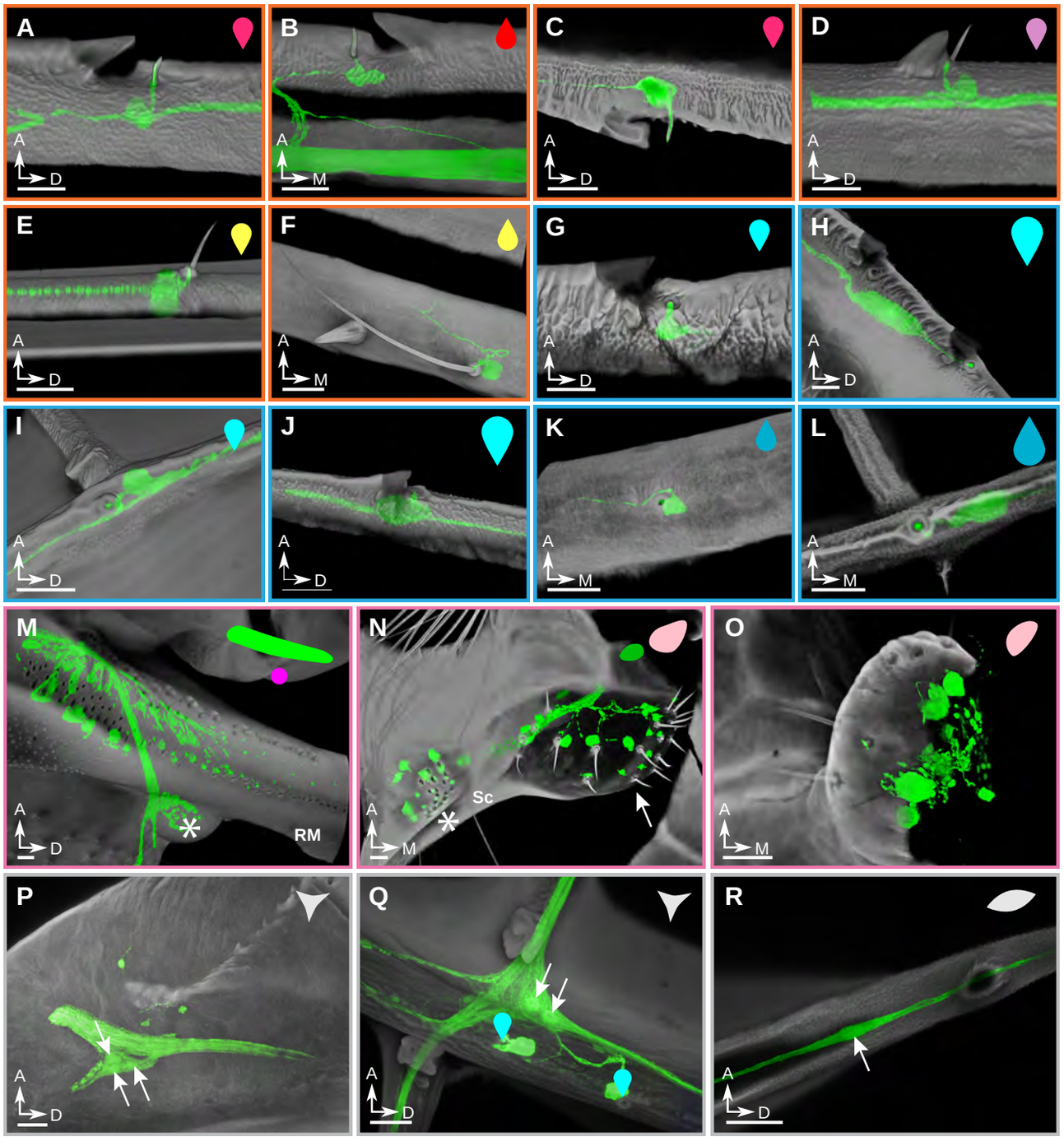

Figure 2: The classification and morphology of all wing sensors
Examples of sensors found on the wings of the dragonfly Perithemis tenera. The scale bars are all 25 µm. (A-F): candidate airflow sensors; (A) dorsal costa bristle-bump; (B) ventral costa bristle-bump; (C) trailing edge bristle-bumps. All three examples show the double-innervated type of a bristle which consist only 25% of all the wing margin bristles. All other bristles have only one dendrite innervating the bristle base (not shown). (D) radius bristle-bump; all bristles of this type are innervated by one neuron at the base. (E) long bristle of the type present on the medial part of several major veins. (F) short bristle. (G-L): strain sensors; (G) dorsal costa campaniform sensillum (CS); (H) large dorsal costa CS; (I) dorsal cross vein CS; (J) large radius anterior CS immediately distal to pterostigma; (K) ventral subcosta CS; (L) terminal ventral CS of the radius posterior 1 (RP1) vein. (M-O): wing base sensory fields; (M) – crevice organ – two parallel fields of directionally tuned elliptical CS at the base of radius/media (RM) vein. Asterisk marks the dorsal insertion site of a wing base chordotonal organ; (N) hair plate (arrow) and two adjacent CS fields (asterisk) ventrally at the base of subcosta; (O) hair plate ventrally at the base of cubitus. (P-R): multipolar and bipolar receptors: (P) multipolar receptor at the base of costa; arrows point to/indicate cell bodies; (Q) multipolar receptor located at the junction of the anal vein and the first/medial cross vein connecting it to cubitus. Two adjacent dorsal CS are indicated with cyan markers. (R) A bipolar receptor. All example images are from the right forewing, with cuticular autofluorescence in grey, and neurons labelled with Neurobiotin/Dyelight-584-Neutravidin in green. The symbols in the upper right corner of each panel are notations to show sensor type and dorsal/ventral placement which will be used in Fig 3.

The thickest longitudinal veins (subcosta, radius, cubitus, media) contain short (10 –15 µm) bristles, each paired with small saw-tooth shaped bump (Figure 2D). The shape of these paired bumps is highly constant across the wing, and across multiple species, as is the spatial relationship between the bump and bristle. Each bristle lies several micrometres distal from the bump, which protrudes from the vein at a shallow gradient on its medial side, and a steep gradient on its distal side. The bump itself is not innervated by a sensory neuron, and thus plays no direct sensory role. However, it will have a conditioning effect on the external flow stimulus acting on the bristle, contributing to the tuning properties of the sensor. The bump might also play a protective role for the small bristles, functioning like a roll cage, preventing collisions from damaging the sensor arrays. To our knowledge, this bristle-bump sensory complex is novel and has not been described in any other animal.

A variety of strain sensitive campaniform sensilla are found on the costa (Figure 2G,H), and several other longitudinal veins (Figure 2I-L), often paired with the same type of saw-toothed cuticular bumps described for short bristles. On many of the joints connecting the radius longitudinal vein to cross veins, we observe isolated campaniform sensilla (Figure 2L), and at the base of the radius we see large fields of campaniform sensilla, each with an associated sensory neuron (Figure 2M). These sensor fields on the radius vein match those described by Simmons (1978), which were described as crevice organs at the time because they resemble pits on the cuticle. Fields of campaniforms with high aspect ratio pits are associated with directional strain sensing (Spinola and Chapman, 1975; Vincent et al., 2007; Zill and Moran 1981). In dipteran flies campaniform sensilla are found on both the wings and the halteres (Cole and Palka, 1982). We also identify several hair plates on the wing base (Figure 2N,O), as well as a chordotonal organ (Figure 2P). These sensory structures are typically associated with proprioception in insects (Kutsch et al., 1980; Burrows, 1996). Finally, we observe multiple multipolar neurons located at some joints between wing veins (Figure 2Q,R) with unknown function and no obvious associated cuticular structure.

A complete sensor map of Odonata wings

Aeroelastic loading of the wing during flight causes complex deformation of the architecture (e.g., Wootton et al., 1998; Norris et al., 2010; Lu et al., 2010, Jongerius and Lentink, 2010). The flow patterns which have been observed on the wings of dragonflies during flight are similarly complex ((e.g.,Thomas et al., 2004; Wang & Sun, 2005; Bomphrey et al., 2016; Li and Dong, 2017; Bode-Oke at al., 2017; Bode-Oke et al., 2018; Hefler et al., 2018; Shumway et al., 2020). We expect the local placement and overall density of wing sensors is critical for capturing relevant information. This system may be a great example of so-called 'fly-by-feel' strategies in biology, in which mechanosensors on the wing directly inform control strategies either in real-time or by providing a training signal for fine-tuning a flight controller. Our imaging data allowed us to construct a complete sensory map of the dragonfly wing (Figure 3) in order to generate hypotheses of how a fly-by-feel controller might receive salient information.

Excluding the wing-base campaniform fields, we found a total of 771 on the forewing and 894 sensors on the hindwing of a dragonfly (*Perithemis tenera*), and 358 sensors on the hindwing of a damselfly (*Argia apicalis*). Extrapolating from this, we estimate this dragonfly has over 3000 wing sensors on its four wings, and the damselfly approximately half as many. Even though this is a very small species of dragonfly, these sensor counts are significantly higher than those reported on the wings of moths, flies or beetles described so far (Dickerson et al., 2014; Cole and Palka, 1982; Frantsevich et al., 2014). The dorsal side of the grasshopper wings were mapped previously, showing sensor counts comparable to those of the dragonfly (Albert et al., 1976). Similarly, large number of sensory bristles have been found on locusts' hindwings (Altman et al., 1978). It is generally a challenge to perform direct cross-species comparison as most sensor maps to date are incomplete in the sensor types and/or coverage.

Several patterns emerged from our complete odonate wing maps. First, sensor type was clearly associated with wing corrugation; for example, long trichoid sensilla are almost exclusively found in the wing's local valleys, while short bristles and bristle-bumps lie on local ridges. This arrangement

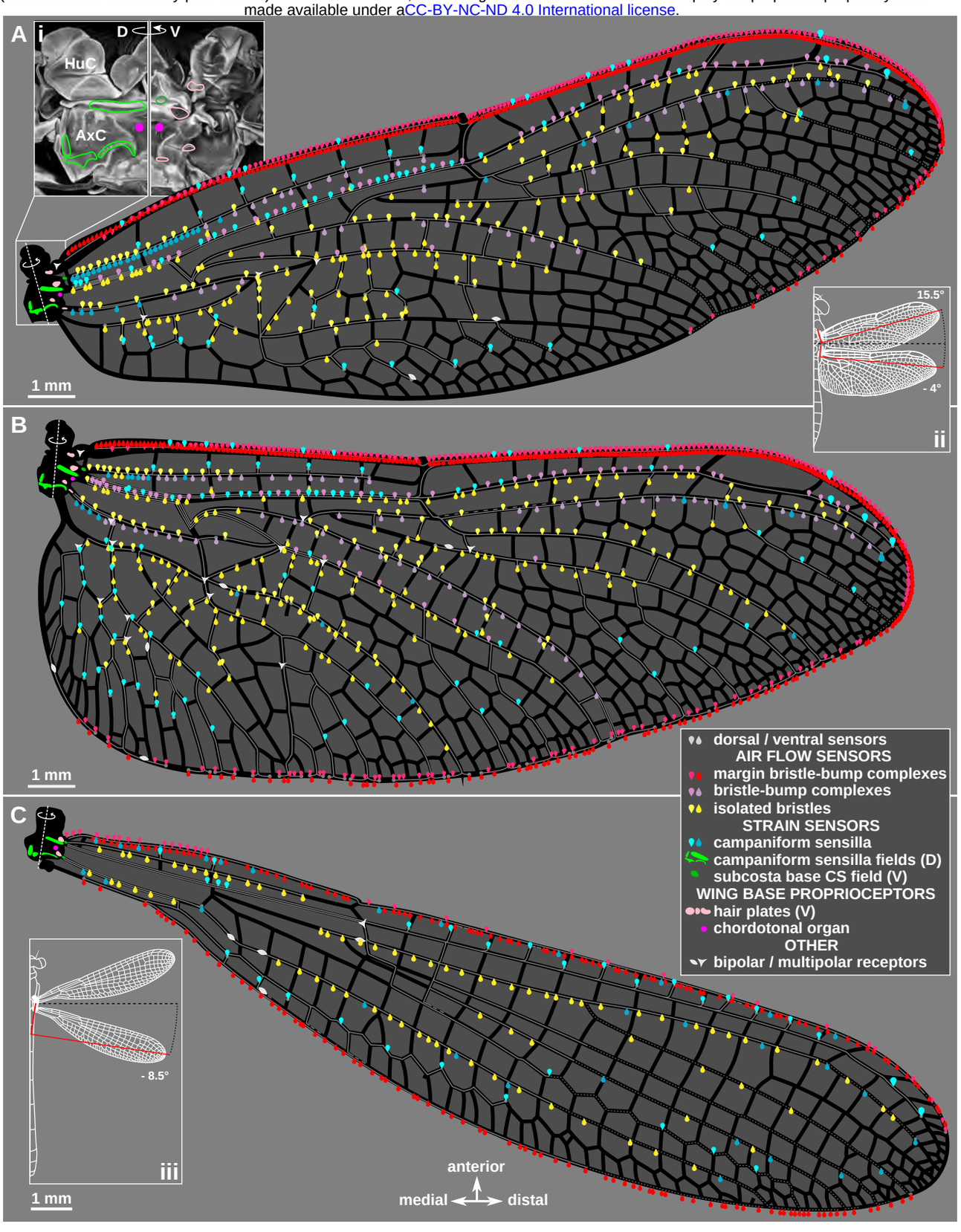

Figure 3: A sensory map of Odonate wings
Distribution of all confirmed sensors on the Perithemis tenera dragonfly fore- (A) and hind (B) wings and a hindwing of Argia apicalis damselfly (C). All sensor notations follow Fig 2 and also in the figure legend. Inset i: maximum intensity projection showing P. tenera right forewing base dorsally and ventrally with the sensor fields outlined. Insets ii and iii: diagrams showing the wings' natural sweep angles; the red reference lines mark the wing span axis perpendicular to the anatomical wing hinges.

could be suitable to detect the small eddies found within the corrugations as well as the attachment state of airflow (Bomphrey et al., 2016). Bristles without any bump dominate the central part of the wing blade in both the dragonfly and the damselfly. The length of these bristles varies ten-fold with bristle length decreasing from the wing base to the wing tip. Since the air speed increases from wing root to wing tip during flapping flight, the boundary layer may also reduce in thickness toward the wing tip. Therefore, the reduction of sensory bristle length may be consistent with the reducing boundary layer height toward the wing tip during flapping flight.

Secondly, the isolated campaniform sensilla are sparsely distributed around the edge of the wing. This ring-like arrangement is consistent with capturing the twist of the wing blade efficiently, as the largest deformations occur at a distance from the axis of twist (Mohren et al., 2018; Koehler et al., 2012). Periodic campaniform sensilla are found along the costa, yet the most posterior campaniform sensilla are located some distance away from the actual trailing edge. This distancing from the trailing edge may prevent wing wear from damaging sensors, and reduce noise from trailing edge aeroelastic flutters. We found a total of 84 and 98 isolated campaniform sensilla on fore and hindwing of *Perithemis tenera*, respectively, with a substantial bias towards the dorsal surface. The abundance of each sensor type varies considerably, bristles significantly outweigh campaniform sensilla on most veins. Interestingly, the damselfly wings studied are completely devoid of bristle bumps, or long bristles (Figure 3c).

Thirdly, both the leading and trailing edges are densely lined with sensory bristles. These are by far the most abundant, accounting for approximately 60% of all wing sensors. Dragonflies generate a strong leading-edge vortex which is shed at the end of each flapping half cycle (Thomas et al., 2004; Bomphrey et al. 2016). Consequently, the wing edges in flapping flight tend to experience large pressure gradients (see e.g., Shumway et al., 2020) and likely experience cyclic changes of airflow direction. The bristles on the wing margin may, therefore, play a key role in observing the timing and intensity of vortex formation and shedding. Similar sensors exist in the moth and have been shown to encode directional vibratory airflow (Ai et al., 2010). In the dragonfly, these sensory bristles are absent in the proximal 2/3rds of the forewing trailing edge. This area of absence matches the area of hindwing overlap during a flapping cycle. This pattern has been observed in the wing margin bristles of a butterfly's forewing and hindwing (Yoshida et al., 2001), suggesting a possible universal strategy to avoid unwanted signals from wing collision.

Fourthly, in general wing sensors are placed with increasing sparsity from anterior to posterior, and from medial to distal. Each sensor has a cost in terms of wing mass, metabolic energy, and carries increased complexity for decoding. For this reason, we expect biological sensor arrays will use the sparsest sensor arrangements that provide sufficient performance with adequate robustness. Simulations of sparse strain sensor systems show that performance is strongly dependent on sensor placement, with optimised sensor arrays resulting in significant reduction in the required number of sensors (Mohren et al., 2018). Mechanical stress on flapping wings is largest close to the wing base, and the metabolic cost of neuronal signalling increases in proportion to the length of an axon, therefore a bias towards medial sensor placement is likely to increase the efficiency of the sensory system.

Finally, the radius and axillary complex at the wing base are adorned with five fields of campaniform sensilla with 30–90 sensors per cluster (Figure 3A, inset). Both structures are load bearing and transmit most of the aerodynamic forces from the wings to the body. These sensilla have high aspect ratios, indicating high directional selectivity. Sensor orientations vary within each field, which might reflect the pattern in the wing base loading during both flapping and gliding flight. There are a handful of multipolar cells scattered at specific cross-vein locations with no associated external structures and, as such, we do not include them for discussion here. Their function remains to be clarified.

Two reasons might justify the Odonates' extensive investment in mechanosensors on their wings. Firstly, dragonfly wings are relatively long, and the intensity of several interesting aerodynamic events

(such as formation of the leading-edge vortex, or shedding of the wing tip vortex) is greater near the wing tip. Sensing these flows using a dense array of wing tip sensors with long and costly axons might be necessary to achieve accurate fly-by-feel control. Secondly, flying insects have a dedicated pump which circulates hemolymph through their wings, often all the way to the wing tip, to support neurons inside these veins (Jensen, 1976; Pass, 2018; Salcedo et and Socha, 2020). This circulation likely makes up a large proportion of the additional mass associated with wing sensing, and once established, in relative terms, the cost of additional sensors and their paired neurons might be insignificant. For these reasons we believe the cost-to-benefit relationship underlying sensor counts is likely to be highly non-linear, and a relatively dense sensor arrangement might be beneficial for some wings.

A comparison of sensor distribution across Odonate families

Odonates are a diverse insect family related to the first flying insects, with wingspans, wingbeat frequencies and flight speeds varying significantly across species (Bomphrey et al., 2016). Are the classes and positioning of wing mechanosensors consistent across different families of Odonata? And how do sensor systems scale as wing sizes vary across odonate species? By performing a broad comparison of wing sensor distribution, we can identify key parameters that are conserved, and expression patterns that might hint at specialised functional roles. We imaged the morphology of wing sensors in 14 species from 10 of the most abundant families of Odonates by exciting autofluorescence under a confocal microscope. From these images we were able to calculate the local sensor density (sensor/mm) along the wing span for each species. To facilitate comparison between species, we normalised each density curve by its respective mean. Our analysis focuses on the costa, subcosta and radius veinsas they contain the most diverse range of sensors, take up most of the load, and play a key role in active wing feathering control (Büsse & Hörnschemeyer, 2013; Wootton, 1992).

On the costa, margin bristle density is quite constant across the wing length for all species on both dorsal and ventral wing surfaces (Figure 4A). However, the damselflies *I. verticalis*, *C. maculata* and the dragonflies *P. tenera*, *S. plagiatus* and *I. stevensi* show local peaks near the nodus (approximately half wing length) on the dorsal side. Interestingly, for all species but *P. gigantea* the average sensor density on the ventral side is higher than on the dorsal side (Table S1). Overall, smaller wings tend to have higher sensor density, with *I. verticalis*, *P. tenera* and *I. stevensi* having an average density of 7 sensors/mm, 8 sensors/mm and 10 sensors/mm respectively compared to 4 sensors/mm average density for *A. sieboldii* and *H. brevistylus* on the dorsal side. Campaniform sensilla density along the major veins exhibits a consistent tapering toward the wing tip (Figure 4B,D,G). Given that strain during flapping decreases from wing hinge to wing tip, this accompanying reduction in campaniform density might be matched to the dynamic range of sensor input (Vincent et al., 2007). We also found occasional campaniform pairs on the major veins. There are a number of explanations: 1) two sensors at the same location provides redundancy; 2) two sensors provides enhanced dynamic range at that location; 3) two sensors can provide dynamic information with spike timing (e.g. direction of deformation propagation); 4) the two-sensor occurrence is simply a result of partially stochastic sensor placement during development with no functional significance. On-going modelling work will narrow down these possibilities in future studies.

The general rule for sensor placement in the valleys and ridges is conserved across species with bristle-bump complexes and campaniform sensilla on the ridges (ventral side of subcosta and dorsal side of radius) and isolated bristles in the valleys (dorsal side subcosta and ventral side radius). Other than the costa, the radius is the most innervated vein and also closest to the torsional axis in a dragonfly wing (Norberg, 1972). The dorsal (ridge side) bristle-bump complexes have a consistent distribution across species (cross species average 2.36 sensors/mm +- 0.49 sensors/mm). It starts with approximately 1.5 normalised sensor density, tapering down to <1, before increasing a little, back to approximately 1.1 normalised sensor density toward the wing tip (Figure 4F). Campaniform sensilla are exclusively located on the dorsal (ridge) side of the radius and paint the most dramatic trend of exponential density reduction with distance from the wing root (Figure 4G).

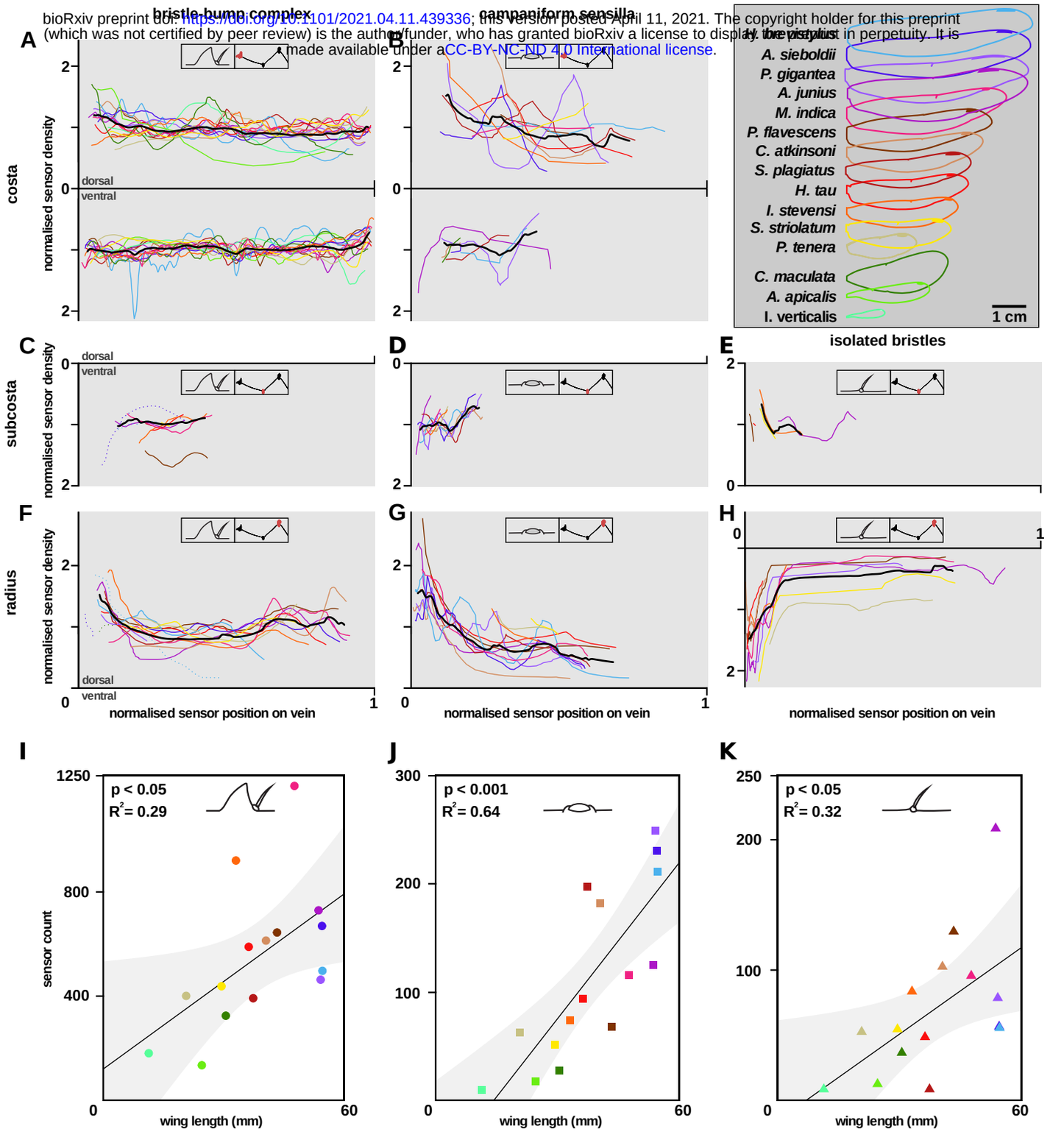

Figure 4: A comparison of sensor distribution across dragonfly families
Sensor density distribution (A-H) and sensor count (I-K) of the wing sensor types (bristle-bump, campaniform sensilla and isolated bristles) across 15 Odonate species. Normalised sensor density is shown for dorsal and ventral side over normalised sensor position on three longitudinal veins, costa (A,B), subcosta (C,D,E) and radius (F,G,H). The insets in each panel highlight sensor type and the respective vein. Sensor density is normalized by the mean of each density curve. Sensor position is normalised by the length of the respective right forewing. The black bold line shows the mean of all species in each plot. (I-K) Sensor count is the sum for each sensor type of all three longitudinal veins. The sensor count is plotted over the respective wing length for each species. Black line shows the ordinary least squares (OLS) regression line and the grey shaded area shows the confidence interval. Each data point is colour coded by the respective species (see legend in upper right panel).

The cross species comparison also shows a positive scaling of sensor count with wing length for all three sensor types (Figure 4I-K). While some smaller Odonates tend to have higher average sensor densities of bristle-bump complexes in the costa, the overall sensor count still increases significantly with wing length (Figure 4I). The strongest linear relationship is found for campaniform sensilla (Figure 4J). This trend is shown further by all three damselfly species (*C. maculata*, *A. apicalis* and *I. verticalis*) having very few (or zero) campaniform sensilla on the costa (Table S1). In general, this suggests that there exists physical rules about sensor counts and larger wings are not simply a scaled up version of the same wing even within odonata. The wing sensory system is well-poised to reconstruct the wing states in addition to providing inertial state estimation for the body.

The strain distribution on major veins and wing state estimation

Campaniform sensilla are strain detectors, but due to signalling limitations they cannot provide a continuous strain value measurement. Instead, they fire an action potential when subjected to strain surpassing their threshold at certain speed. A suitable distribution of campaniform sensilla is important for providing information on the gross strain distribution on wing veins under normal operation. Previous work has focused on the placement of wing campaniform sensilla in the context of inertial sensing of body rotations (Eberle et al., 2015; Pratt et al., 2017). Specifically, it has been demonstrated that only relatively few, sparsely distributed strain sensors are needed to detect rotations of the body (Hinson and Morgansen, 2015). This is certainly consistent with the sparse distribution of campaniform sensilla found in some model insects (e.g., flies: Dickinson and Palka, 1987). Here we have revealed a relatively denser distribution of campaniform along some major wing veins in Odonates. How might these elaborate sensor systems inform flight behaviour? One idea is that the higher strain sensor density facilitates the monitoring of complex wing states.

Given a wing structure's mechanical properties, the strain distribution along the major veins is determined by the sum of inertial and aerodynamic loads. When flapping, inertial loads generally exceed the aerodynamic loads for large insects (e.g., Combes & Daniel, 2003; Jankauski et al., 2017). To encode any aerodynamic components of stain, the wing sensory system must differentiate small variations of the strain field from the dominant inertial load. Understanding this requires examining some possible wing states and their representative strain fields on the veins. We generated some possible wing states without the fluid-solid interactions by building a computational solid dynamics (CSD) model of a flapping *S. striolatum* dragonfly wing via our µCT data (see Methods).

The surface spanwise strain contours of four snapshots (Figure 5A–D) show the concentration of high strain magnitudes at the longitudinal veins near the wing base. The spanwise strain is greatest at the stroke reversals (pronation and supination) while the sign for each longitudinal vein is mostly reversed (Figure 5A,C): e.g., the proximal portion of the radius experiences compression (negative strain, in blue) at pronation (Figure 5A), while the same vein experiences tension (positive strain, in red) at supination (Figure 5C). On the other hand, proximal subcosta and cubitus (two longitudinal veins adjacent to radius) are showing the opposite trends. This is presumably because the corrugation offsets some longitudinal veins away from the neutral plane of bending. We also quantified the spanwise strain along the surface of two major longitudinal veins (subcosta and radius, Figure 5E–J) where we found many campaniform sensilla on their corresponding "ridge" sides (ventral side for subcostal and dorsal side for radius). These veins show a consistent pattern of strain distribution along their length throughout the flapping cycle (Figure 5G,H), but with a large variation in magnitude with time (Figure 5I,J). To resolve any shape variations in the strain pattern, we normalized the strain magnitude at a range of instants throughout the cycle.

How might the wing sensory system encode real-time features of wing kinematics? If the strain on the veins is a reliable proxy for the instantaneous aeroelastic loading on the wing, and the nominal inherent strain distribution is known, then the description of the wing state can be broken down into two components: 1) magnitude of inherent strain distribution; and 2) the state-specific deviation from the nominal strain distribution. The first component requires relatively few sensors in few locations:

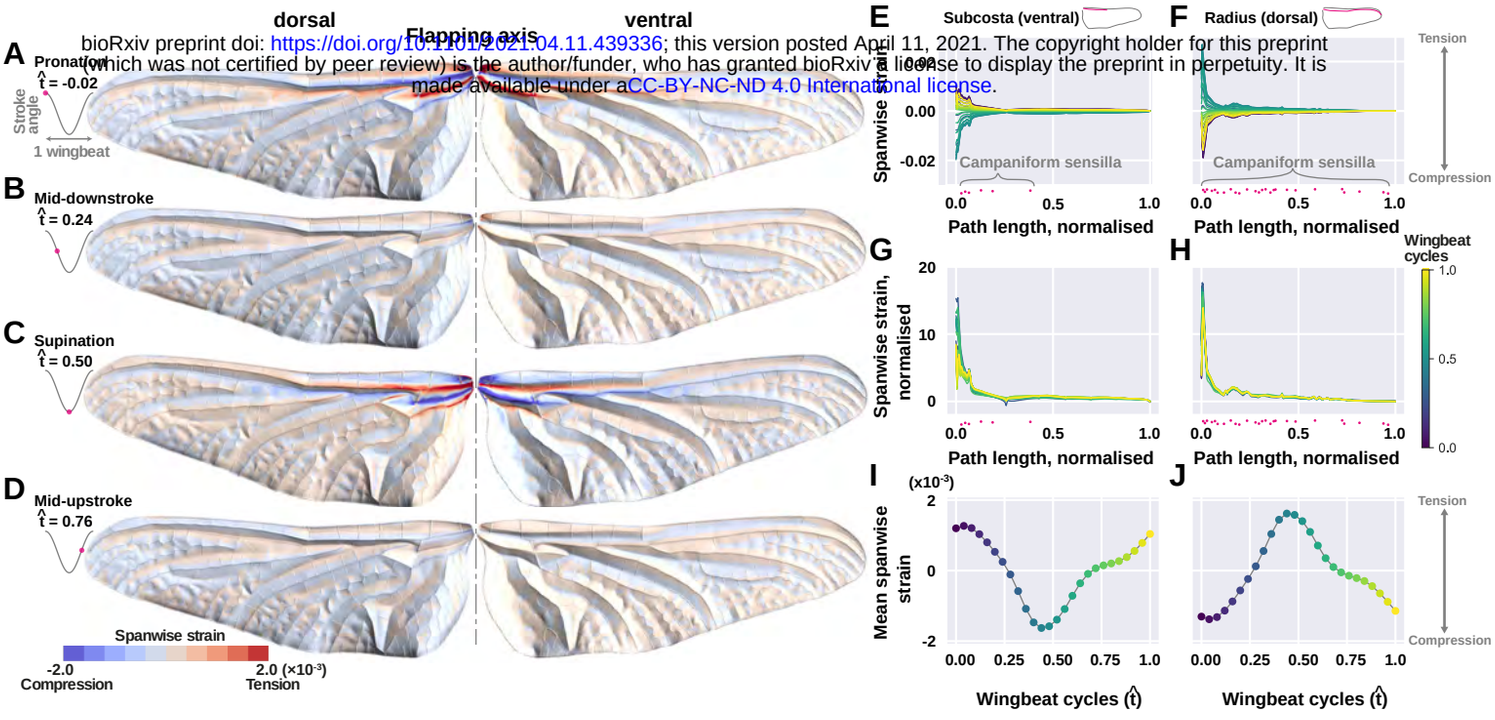

Figure 5: Strain distributions on a simulated flapping wing

(A–D) Spanwise strain (spanwise component of normal elastic strain) contour over the wing surface for four time instances in a wing stroke cycle: pronation (A), mid-downstroke (B), supination (C), and mid-upstroke (D). A hindwing of a Sympetrum striolatum was reconstructed in 3D for this simulation. (E,F) Spanwise strain along ventral subcosta and dorsal radius where campaniform sensilla can be found. The colour map represents different phase of a flapping cycle. (G,H) Spanwise strains along the veins, each line is normalised with the mean of the strain along the vein . The x-axis (path length, or position along vein) for the spanwise strains are normalised with the total path length for corresponding vein. (I,J) Temporal variation of the mean spanwise strain on the ventral subcosta and dorsal radius. The measured positions of campaniform sensilla are shown in magenta dots (E,F,G,H). The vertical variation of the dots is purely for readability.

just enough for the system to be robust. Any deviation from the nominal profile provides a signature for the wing deformation state that could be caused by perturbations or altered kinematics, for example, when manoeuvring. Thus, the second component requires sampling the strain magnitude with high spatial resolution, which can be accomplished by increasing the campaniform count. Specifically, since campaniform function as a strain detector, any location experiencing large fluctuation of strain might need more campaniform with different strain thresholds and temporal tuning. Alternatively, any variation in strain magnitude can be encoded in the phase of a high density of similar campaniform. Again, in area where large strain sensing range is required, we expect larger number of campaniform. While the reconstructed strain magnitude match the expectation of the observed campaniform density, ongoing electrophysiological studies aim to differentiate between the two hypotheses.

The nominal inherent strain distribution is largely determined by the wing architecture and flapping modes. The insect likely has a good expectation/prediction about this distribution from which it identifies abnormalities. While the wing mechanical properties are relatively constant once the wings have hardened following eclosion (but see Salcedo & Socha, 2020 for potential roles of hemolymph), any damage that alters the wing's structural mechanics will cause a permanent change to the nominal profile. Consequently, the expectation of this nominal strain distribution must be updated.

Conclusion

This work provides the first complete map of wing sensory system for any flying animal from neuron wiring to sensor morphology and distribution. We have also discovered novel sensors with their functions still under ongoing investigation. The cross-species comparison has revealed what appear to be conserved sensor placement themes that may be key to understanding the fly-by-feel controller. Finally, our initial geometrically precise structural dynamics modeling generated hypotheses for the distributed strain sensors to monitor wing states. Our findings raise several key questions regarding aeroelastic sensing for flight control. These will be investigated with follow-up neurophysiological experimentation and computational fluid-structure interaction modelling.

Insect wings are underactuated yet extensively sensorised structures. Their venation patterns must not only produce predictable passive mechanical behaviours, but also provide an appropriate substrate to support the number, density, and appropriate positioning of wing sensors in order to observe the relevant forces during flight. To add yet more complexity, it is feasible and likely, that the vein substrates are mechanically tuned to amplify, or filter, the response of the sensors they support. This hand-in-glove integration of mechanical behaviour and sensing for state estimation makes insect wings an intriguing and tractable model for investigating the co-evolution of form, function, and the nervous system.

Author contributions

HTL & RJB conceived the project and secured funding; JF & HTL performed pilot studies and preliminary mapping; IS performed the staining, confocal microscopy, and generated the neuroanatomy maps; IS and MU analysed the sensor distribution data; MM built the wing model and performed the flapping simulation. JF & HTL developed the manuscript; all authors revised the manuscript for submission.

Acknowledgements

We would like to thank the Biotechnology and Biological Sciences Research Council for supporting this work (Grant BB/R002509/1 to HTL and BB/R002657/1 to RJB). We would like to thank Dr Ben Price for lending us selected specimens from the NHM collection. We lament the environmental destruction for housing development at one of our dragonfly sites in SE England. Habitat loss has always been the biggest impact to wild animals.

Methods

Insect specimens

All Odonate specimens were collected in northern Virginia, USA (*), south-east England, UK (**), or obtained from the collection at the Natural History Museum in London, UK. They belong to two suborders: first, Anisoptera, the dragonflies, of which there are 13 families; members of the nine most populous/largest were studied here: 1. Aeshnidae, *Anax junius* (Drury, 1773)*, 2. Chlorogomphidae, *Chlorogompus atkinsonii* (Fraser, 1925), 3. Cordulegastridae, *Anotogaster seiboldii* (Selys, 1854), 4. Corduliidae, *Hemicordulia tau* (Selys, 1871), 5. Gomphidae, *Hagenius brevistylus* (Selys, 1854) and *Stylyrus plagiatus* (Selys, 1854)*, 6. Macromiidae, *Macromia indica* (Frasner, 1924), 7. Libellulidae, *Pantala flavescens* (Fabricius, 1798)*, *Perithemis tenera* (Say, 1840)*and *Sympetrum striolatum* (Charpentier, 1840)**, 8. Petaluridae, *Petalura gigantea* (Leach. 1815), 9. Synthemistidae, *Idionyx stevensi* (Fraser, 1924). Second, Zygoptera, the damselflies, of which there are 35 families. The damselflies used here were from the 1. Calopterigidae, *Calopteryx maculata* (Palisot de Beauvois, 1807)* and 2. Coenagrionidae, *Argia apicalis* (Say, 1840)* and *Ischnura verticalis* (Say, 1839)*. We used males in all our analyses, except for *P. tenera*, for which we used both males and females. There are no evident morphological differences in the wings between sexes except for pigmentation.

Sample preparation for confocal imaging

To obtain a more complete neuronal tracing, it is best to minimize sample segmentation. Neurobiotin diffuses at a rate of ~1 cm/24 hr in axons of the diameter found in the odonate wing, and insect tissue deterioration begins at approximately 48 hr postmortem. Thus we focused our efforts on one of the smallest anisopteran species, *P. tenera*, and an isopteran, *A. apicalis*, with comparable wing length.

Insects were anesthetized on ice and fixed right side up on Sylgard-filled Petri dishes using pins. The right pterothoracic pleural wall and the head were removed, anterior nerves (nerves 1C and 2C in Simmons, 1977) were isolated, placed in a drop (~ 0.7 µl) of distilled water inside a petroleum jelly bowl, and cut. Water was wicked away, replaced with ~0.5 µl of the tracer solution (2 % w/v neurobiotin in dH_2O, Vector Labs, SP-1120) and the well was sealed closed with petroleum jelly. Insects were kept refrigerated in a humid chamber for 48 hours to allow diffusion of the tracer. The wings were removed by cutting along the basal hinge and fixed in 2% PFA in phosphate-buffered saline with 0.1% Triton X-100 (PBS-T) overnight at 4°C with mild agitation, washed with PBS-T and bleached in 20% peroxide in PBS-T for 48 h to remove most of the pigment from the cuticle.

When wings harvested from young, probably not more than few hours post-eclosion, adults were used, minutes after commencement of bleaching bubbles of oxygen started appearing within the bilayer of cuticle making up the wing blade. This can be explained by the presence of metabolites between the yet-unfused sheets of exoskeleton capable of catalyzing the decomposition of peroxide. At the point of completion of bleaching, indicated by the cuticle's pale golden hues, the wings took appearance of a rescue buoy. The wings were briefly rinsed in copious amount of water and, while floating in a PBS-T-filled Petri dish, placed inside a desiccator connected to a rotary vane pump. The negative gauge pressure caused further delamination of the cuticular bilayer and the gas to escape via the openings at the wing base or, in some cases, ruptured trailing edge seam. The wings were cut chordwise in half, post-fixed in 2 % PFA for 3 h @ RT, washed and stained with DyLight 594-NeutrAvidin (1:250, Thermo Scientific #22842), now having free/unencumbered access to the neurobiotin-labelled neurons, in PBS with 3% normal goat serum, 1% triton X-100, 0.5% DMSO @ RT with agitation for 2 days. Following washing with PBS-T, the wings were cut near their base and mounted in Tris-buffered (50 mM, pH 8.0) 80% glycerol with 0.5 % DMSO between two coverslips using 350 µm spacers. The wing bases were dehydrated in glycerol (5-80 %), then ethanol (25-100 %) series, cleared and mounted in methyl salicylate, following modified protocol from Ott, 2008.

For treatments of old wing specimens, samples were bleached and re-hydrated using alkaline peroxide (25% H_2O_2, 0.2% KOH in water) for 24-48 h and mounted in Tris-buffered (50 mM, pH 8.0) 80% glycerol

with 0.5 % DMSO between two 60 mm-long coverslips. The mounting followed the same procedure as fresh wings.

Imaging and sensor distribution/placement mapping

All samples were imaged on Zeiss 880 upright confocal microscope. Serial optical sections were obtained at 7 µm with a FLUAR 5x/0.25 NA, 2.5 µm with a Plan-Apochromat 10x/0.45 NA objective, at 1.5 µm with a LD-LCI 25x/0.8 NA objective or at 0.5 µm with a Plan-Apochromat 40x/0.8 NA objective. Cuticle autofluorescence and DyLight 594-NeutrAvidin were imaged using 488 and 594 nm laser lines, respectively. The volumes obtained with the FLUAR 5x objective and tiling the wings were stitched in Fiji (http://fiji.sc/). Images were processed in Fiji, Icy (http://icy.bioimageanalysis.org/) and Photoshop (Adobe Systems Inc.).

The costa, radius and subcosta veins were scanned dorsally and ventrally with Plan-Apochromat 10x/0.45 NA objective (field of view 1.2 x 1.2 mm). To minimize collection time while maintaining high signal to noise ratio, the green autofluorescence of cuticle was excited with 405 and 488 nm lasers at maximum power and the images were collected using single-swipe and minimum pixel dwell time. The vertical aspect of each volume was adjusted to accommodate the imaged vein while the horizontal was kept constant at 1500 pixels. Maximum intensity projections were stitched manually in Photoshop and annotated in Adobe Illustrator (Adobe Systems Inc.) while referring to the volumes viewed in Fiji (Schindelin et al., 2012).

Wing sensor distribution quantifications

Based on the annotations, sensors were counted and their position on the wing tracked in Fiji. The distance between sensors of the same type was measured and the inverse of the sensor distance was taken (sensors/mm). The sensor density was averaged over two consecutive distances to get the local sensor density at each sensor position. The sensor position was normalised with the wing length for comparison across species. Sensor density was first smoothed by a moving average over 7 data points and subsequently normalised by the mean sensor density of the respective sensor type on the vein. Further, the mean of all species was taken for each sensor type to compare sensor density curves across sensor type and veins.

The relationship between sensor count and wing length for each sensor type was analysed via an ordinary least squares (OLS) regression in Rstudio (Rstudio Team, 2020). The lower and upper confidence interval (2.5% and 97.5%) of the OLS regression was calculated. The sensor count for each sensor type corresponds to the sum of the sensors of the first three anterior veins (costa, subcosta and radius).

Wing geometry modelling for strain field evaluation

A male *Sympetrum striolatum* dragonfly was euthanised in a freezer overnight. The entire body was stained with contrast agent elemental iodine in a glass jar which had a desiccating effect (Boyde et al., 2014). The x-ray microtomography (µCT) scanning on the left hindwing was performed using a SkyScan 1172 scanner (Bruker, Belgium). The wing mounting was aligned to the vertical direction (rotational axis) and 5 sub-scans were performed. With the rotation step of 0.08° for 180° rotation for each sub-scan, in total 12445 images were taken at pixel size of 2.83 µm and exposure time of 2.6 s. The source voltage and current were 65 kV and 153 µA, respectively. The raw images were processed in Bruker NRecon to obtain the cross-sectional slices. The images were then imported to ORS Dragonfly v3.6 (Object Research Systems, Canada) for registration and three-dimensional reconstruction. A mesh file (PLY) was extracted by choosing an appropriate intensity threshold. After cleaning and reduction in MeshLab, the mesh was imported to Rhinoceros 6 (Robert McNeel & Associates, USA). The vein network was approximated with circular cross-sectional pipes whose diameter and positions of the joints were informed from the mesh. The membrane was generated for each cell surrounded by veins with uniform thickness of 10 µm, which was determined based on the sampling in the CT scanned cross section in Dragonfly software. The veins and membranes were imported into AutoDesk Inventor

Professional 2020 (Autodesk, Inc., USA) to merge them into one single body. The wing model was exported in STEP format and imported into ANSYS Mechanical Application 2019 R3 (ANSYS, Inc., USA), where the mesh for finite element analysis was generated and transient structural simulation was performed.

Wing flapping computational solid dynamics (CSD) simulation

The wing model mesh consists of quadratic tetrahedron elements with the total number of nodes of 0.8 million. The uniform material property was assumed for simplicity, where density was 1200 kg m^{-3}, Poisson ratio was 0.3, and the Young's modulus was 5 GPa. These values were derived from previous work (Jongerius and Lentink, 2010), where the Young's moduli were 6 GPa for vein and 3.75 GPa for membrane. The "remote displacement" boundary condition was applied at the wingbase surface, where only 1 degree of freedom for rotation was prescribed for simulating the flapping motion, and other 5 (3 translational and 2 rotational) degrees of freedom were fixed to be zero. The flapping motion is described as:

$$\phi = \phi_0 \sin(2\pi t f)\,(1 - e^{-\gamma t})$$

where ϕ is positional angle given at the wingbase in degrees, ϕ_0 is the desired wingbeat semi-amplitude and set to 30°, t is time in seconds, f is wingbeat frequency and set to 40 Hz, and γ is a factor to change how fast the amplitude approaches to ϕ_0. The wingbeat amplitude increases gradually in this formulation so we can avoid the abrupt start and it is expected to arrive at the periodic deformation state earlier than a simple sinusoidal flapping. The factor γ was set to 30, which results in the wingbeat amplitude is 30% of ϕ_0 for the 1st cycle but 67%, 84%, and 93% for 2nd, 3rd, and 4th cycles, respectively. At 10th cycle the amplitude is 99.9% of ϕ_0. The wing starts flapping from the mid-downstroke phase at time t = 0, and the computation was performed until time t = 16T= 0.4 s, where T = 1/f is the wingbeat period, which is 0.025 s. The time step size (time increment, Δt) for each computational step was adjusted automatically within the limits between 2×10^{-5} s and 2×10^{-3} s, with the initial size of 2×10^{-4} s. There was no coupling (interaction) with the aerodynamics.

The resultant strain field was evaluated in two ways: the normal elastic strain along two major longitudinal veins (subcosta and radius), and the normal elastic strain contours on the wing surface at four time instances (pronation, mid-downstroke, supination, and mid-upstroke). Here, the normal elastic strain was computed for the wing radial direction for each time instance by two-dimensional coordinate transformation using the instantaneous positional angle. We will refer this strain component as "spanwise strain" for short. The component parallel to the flapping axis is not included in this spanwise strain. Only the last wingbeat cycle starting from pronation (i.e., $14.75 \leq t/T \leq 15.75$) was used for the analysis, and the t/T was renamed for this period as $\hat{t}$ such that $\hat{t} := t/T - 14.75$.

References

Ai, H., Yoshida, A., & Yokohari, F. (2010). Vibration receptive sensilla on the wing margins of the silkworm moth Bombyx mori. *Journal of Insect Physiology*, *56*(3), 236–246. https://doi.org/10.1016/j.jinsphys.2009.10.007

Albert, P. J., Zacharuk, R. Y., & Wong, L. (1976). Structure, innervation, and distribution of sensilla on the wings of a grasshopper. *Canadian Journal of Zoology*, *54*(9). https://doi.org/10.1139/z76-178

Altman, J. S., Anselment, E., & Kutsch, W. (1978). Postembryonic development of an insect sensory system: Ingrowth of axons from hindwing sense organs in Locusta migratoria. *Proceedings of the Royal Society of London - Biological Sciences*, *202*(1149), 497–516. https://doi.org/10.1098/rspb.1978.0082

Bacon, J., & Tyrer, M. (1979). The innervation of the wind-sensitive head hairs of the locust, Schistocerca gregaria. *Physiological Entomology*, *4*(4), 301–309. https://doi.org/10.1111/j.1365-3032.1979.tb00621.x

Bechly, G. (1995). Morphologische Untersuchungen am Flügelgeäder der rezenten Libellen und deren Stammgruppenvertreter (Insecta; Pterygota; Odonata) unter besonderer Berücksichtigung der Phylogenetischen Systematik und des Grundplanes der *Odonata. In *Petalura: Vol. spec.-*. http://ci.nii.ac.jp/naid/10018122864/en/

Bode-Oke, A. T., Zeyghami, S., & Dong, H. (2018). Flying in reverse: kinematics and aerodynamics of a dragonfly in backward free flight. *Journal of The Royal Society Interface*, *15*(143), 20180102. https://doi.org/10.1098/rsif.2018.0102

Bode-Oke, A. T., Zeyghami, S., & Dong, H. (2017). Aerodynamics and flow features of a damselfly in takeoff flight. *Bioinspiration & Biomimetics*, *12*(5), 056006. https://doi.org/10.1088/1748-3190/aa7f52

Bomphrey, R. J., & Godoy-Diana, R. (2018). Insect and insect-inspired aerodynamics: unsteadiness, structural mechanics and flight control. *Current Opinion in Insect Science*, *30*, 26–32. https://doi.org/10.1016/j.cois.2018.08.003

Bomphrey, R. J., Nakata, T., Henningsson, P., & Lin, H.-T. (2016). Flight of the dragonflies and damselflies. *Philosophical Transactions of the Royal Society B: Biological Sciences*, *371*(1704), 20150389. https://doi.org/10.1098/rstb.2015.0389

Bowers, A. H., Murillo, O. J., Jensen, R. R., Eslinger, B., & Gelzer, C. (2016). On Wings of the Minimum Induced Drag: Spanload Implications for Aircraft and Birds. *Nasa/Tp—2016–219072*, *March*, 1–22.

Boyde, A., Mccorkell, F. A., Taylor, G. K., Bomphrey, R. J., & Doube, M. (2014). Iodine vapor staining for atomic number contrast in backscattered electron and X-ray imaging. *Microscopy Research and Technique*, *77*(12), 1044–1051. https://doi.org/10.1002/jemt.22435

Brown, R. E., & Fedde, M. R. (1993). Airflow Sensors in the Avian Wing. *Journal of Experimental Biology*, *179*(1), 13–30.

Burrows, M. (2012). The Neurobiology of an Insect Brain. In *The Neurobiology of an Insect Brain*. https://doi.org/10.1093/acprof:oso/9780198523444.001.0001

Büschges, A., & DiCaprio, R. A. (2008). Somatosensation in Invertebrates. In R. H. Masland, T. D. Albright, T. D. Albright, R. H. Masland, P. Dallos, D. Oertel, S. Firestein, G. K. Beauchamp, M. Catherine Bushnell, A. I. Basbaum, J. H. Kaas, & E. P. Gardner (Eds.), *The Senses: A Comprehensive Reference* (pp. 355–362). Elsevier. https://doi.org/10.1016/B978-012370880-9.00362-5

Büsse, S., & Hörnschemeyer, T. (2013). The thorax musculature of Anisoptera (Insecta: Odonata) nymphs and its evolutionary relevance. *BMC Evolutionary Biology*, *13*(1), 237. https://doi.org/10.1186/1471-2148-13-237

Byrne, B. Y. D. N., Buchmann, S. L., & Spangler, H. G. (1998). Relationship Between Wing Loading, Wingbeat Frequency and Body Mass in Homopterous Insects. *Journal of Experimental Biology*, *135*(1), 9–23.

Camhi, J. M. (1969). Locust wind receptors. I. Transducer mechanics and sensory response. *Journal of Experimental Biology*, *50*(2), 335–348.

Carruthers, A. C., Thomas, A. L. R., & Taylor, G. K. (2007). Automatic aeroelastic devices in the wings of a steppe eagle Aquila nipalensis. *Journal of Experimental Biology*, *210*(23), 4136–4149. https://doi.org/10.1242/jeb.011197

Cole, E. S., & Palka, J. (1982). The pattern of campaniform sensilla on the wing and haltere of Drosophila melanogaster and several of its homeotic mutants. *Journal of Embryology and Experimental Morphology*, *71*, 41–61.

Combes, S. A. (2003). Flexural stiffness in insect wings II. Spatial distribution and dynamic wing bending. *Journal of Experimental Biology*, *206*(17), 2989–2997. https://doi.org/10.1242/jeb.00524

Dickerson, B. H., Aldworth, Z. N., & Daniel, T. L. (2014). Control of moth flight posture is mediated by wing mechanosensory feedback. *Journal of Experimental Biology*, *217*(13), 2301–2308. https://doi.org/10.1242/jeb.103770

Dickinson, M. H. (1990). Comparison of Encoding Properties of. *Journal of Experimental Biology*, *151*, 245–261.

Dickinson, M., & Palka, J. (1987). Physiological properties, time of development, and central projection are correlated in the wing mechanoreceptors of Drosophila. *The Journal of Neuroscience*, *7*(12), 4201–4208. https://doi.org/10.1523/JNEUROSCI.07-12-04201.1987

Dickinson, M. H. (1999). Haltere–mediated equilibrium reflexes of the fruit fly, Drosophila melanogaster. *Philosophical Transactions of the Royal Society of London. Series B: Biological Sciences*, *354*(1385), 903–916. https://doi.org/10.1098/rstb.1999.0442

Dickson, W., Straw, A., Poelma, C., & Dickinson, M. (2006). An Integrative Model of Insect Flight Control (Invited). *44th AIAA Aerospace Sciences Meeting and Exhibit*, *1*(January), 431–449. https://doi.org/10.2514/6.2006-34

Donoughe, S., Crall, J. D., Merz, R. A., & Combes, S. A. (2011). Resilin in dragonfly and damselfly wings and its implications for wing flexibility. *Journal of Morphology*, *272*(12), 1409–1421. https://doi.org/10.1002/jmor.10992

Ellington, C. P., van den Berg, C., Willmott, A. P., & Thomas, A. L. R. (1996). Leading-edge vortices in insect flight. *Nature*, *384*(6610), 626–630. https://doi.org/10.1038/384626a0

Fabian, J. M., el Jundi, B. M., Wiederman, S. D., & O'Carroll, D. C. (2020). The complex optic lobe of dragonflies. *bioRxiv*. https://doi.org/10.1101/2020.05.10.087437

Frantsevich, L., Gorb, S., Radchenko, V., Gladun, D., & Polilov, A. (2014). Lehr's fields of campaniform sensilla in beetles (Coleoptera): Functional morphology. I. General part and allometry. *Arthropod Structure and Development*, *43*(6), 523–535. https://doi.org/10.1016/j.asd.2014.09.001

Gao, C.-Y., Meng, G.-X., Li, X., Wu, M., Liu, Y., Li, X.-Y., Zhao, X., Lee, I., & Feng, X. (2013). Wettability of dragonfly wings: the structure detection and theoretical modeling. *Surface and Interface Analysis*, *45*(2), 650–655. https://doi.org/10.1002/sia.5105

Hefler, C., Qiu, H., & Shyy, W. (2018). Aerodynamic characteristics along the wing span of a dragonfly Pantala flavescens. *The Journal of Experimental Biology*, *221*(19), jeb171199. https://doi.org/10.1242/jeb.171199

Hinson, B. T., & Morgansen, K. A. (2015). Gyroscopic sensing in the wings of the hawkmoth Manduca sexta : the role of sensor location and directional sensitivity. *Bioinspiration & Biomimetics*, *10*(5), 056013. https://doi.org/10.1088/1748-3190/10/5/056013

Houghton, E. L., & Carruthers, N. B. (1982). Aerodynamics for engineering students. Third edition. *Aerodynamics for Engineering Students: Seventh Edition*.

Houot, B., Gigot, V., Robichon, A., & Ferveur, J.-F. (2017). Free flight odor tracking in Drosophila: Effect of wing chemosensors, sex and pheromonal gene regulation. *Scientific Reports*, *7*(1), 40221. https://doi.org/10.1038/srep40221

Humphrey, J. A. C., & Barth, F. G. (2007). Medium Flow-Sensing Hairs: Biomechanics and Models. In *Advances in Insect Physiology* (Vol. 34, Issue 07, pp. 1–80). https://doi.org/10.1016/S0065-2806(07)34001-0

Jongerius, S. R., & Lentink, D. (2010). Structural Analysis of a Dragonfly Wing. *Experimental Mechanics*, *50*(9), 1323–1334. https://doi.org/10.1007/s11340-010-9411-x

546 Keil, T. A. (1997). Functional morphology of insect mechanoreceptors. *Microscopy Research and Technique*,
547 *39*(6), 506–531. https://doi.org/10.1002/(SICI)1097-0029(19971215)39:6<506::AID-JEMT5>3.0.CO;2-B

548 Koehler, C., Liang, Z., Gaston, Z., Wan, H., & Dong, H. (2012). 3D reconstruction and analysis of wing
549 deformation in free-flying dragonflies. *Journal of Experimental Biology*, *215*(17), 3018–3027.
550 https://doi.org/10.1242/jeb.069005

551 Kondo, H. (1978). Efferent system of the lateral ocellus in the dragonfly: Its relationships with the ocellar
552 afferent units, the compound eyes, and the wing sensory system. *Journal of Comparative Physiology ? A*,
553 *125*(4), 341–349. https://doi.org/10.1007/BF00656869

554 Kutsch, W., Hanloser, H., & Reinecke, M. (1980). Light- and electron-microscopic analysis of a complex sensory
555 organ: The tegula of Locusta migratoria. *Cell and Tissue Research*, *210*(3), 461–478.
556 https://doi.org/10.1007/BF00220202

557 Li, C., & Dong, H. (2017). Wing kinematics measurement and aerodynamics of a dragonfly in turning flight.
558 *Bioinspiration & Biomimetics*, *12*(2), 026001. https://doi.org/10.1088/1748-3190/aa5761

559 Li, J., Zhang, W., Guo, Z., Wu, S., Jan, L. Y., & Jan, Y.-N. (2016). A Defensive Kicking Behavior in Response to
560 Mechanical Stimuli Mediated by Drosophila Wing Margin Bristles. *The Journal of Neuroscience*, *36*(44),
561 11275–11282. https://doi.org/10.1523/JNEUROSCI.1416-16.2016

562 May, M. L. (1982). Heat Exchange and Endothermy in Protodonata. *Evolution*, *36*(5), 1051.
563 https://doi.org/10.2307/2408082

564 McCorkell, F. (2016). *Aerodynamic flow sensing in the desert locust (Schistocerca gregaria)*. University of
565 Oxford.

566 Mohren, T. L., Daniel, T. L., Brunton, S. L., & Brunton, B. W. (2018). Neural-inspired sensors enable sparse,
567 efficient classification of spatiotemporal data. *Proceedings of the National Academy of Sciences of the*
568 *United States of America*, *115*(42), 10564–10569. https://doi.org/10.1073/pnas.1808909115

569 Mountcastle, A. M., Alexander, T. M., Switzer, C. M., & Combes, S. A. (2016). Wing wear reduces bumblebee
570 flight performance in a dynamic obstacle course. *Biology Letters*, *12*(6), 20160294.
571 https://doi.org/10.1098/rsbl.2016.0294

572 Nalbach, G. (1993). The halteres of the blowfly Calliphora - I. Kinematics and dynamics. *Journal of Comparative*
573 *Physiology A*, *173*(3), 293–300. https://doi.org/10.1007/BF00212693

574 Niven, J. E., & Laughlin, S. B. (2008). Energy limitation as a selective pressure on the evolution of sensory
575 systems. *Journal of Experimental Biology*, *211*(11), 1792–1804. https://doi.org/10.1242/jeb.017574

576 Norberg, Å. R. (1972). The pterostigma of insect wings an inertial regulator of wing pitch. *Journal of*
577 *Comparative Physiology*, *81*(1), 9–22. https://doi.org/10.1007/BF00693547

578 Pass, G. (2018). Beyond aerodynamics: The critical roles of the circulatory and tracheal systems in maintaining
579 insect wing functionality. In *Arthropod Structure and Development* (Vol. 47, Issue 4, pp. 391–407).
580 Elsevier Ltd. https://doi.org/10.1016/j.asd.2018.05.004

581 Pflüger, H.-J., & Wolf, H. (2013). Developmental and activity-dependent plasticity of filiform hair receptors in
582 the locust. *Frontiers in Physiology*, *4*(August), 1–7. https://doi.org/10.3389/fphys.2013.00070

583 Phan, H. V., Truong, Q. T., & Park, H. C. (2019). Extremely large sweep amplitude enables high wing loading in
584 giant hovering insects. *Bioinspiration & Biomimetics*, *14*(6), 066006. https://doi.org/10.1088/1748-
585 3190/ab3d55

586 Piersanti, S., Frati, F., Conti, E., Gaino, E., Rebora, M., & Salerno, G. (2014). First evidence of the use of olfaction
587 in Odonata behaviour. *Journal of Insect Physiology*, *62*(1), 26–31.
588 https://doi.org/10.1016/j.jinsphys.2014.01.006

589 Pratt, B., Deora, T., Mohren, T., & Daniel, T. (2017). Neural evidence supports a dual sensory-motor role for
590 insect wings. *Proceedings of the Royal Society B: Biological Sciences*, *284*(1862), 20170969.
591 https://doi.org/10.1098/rspb.2017.0969

592 Pringle, J. W. S. (1948). The Gyroscopic Mechanism of the Halteres of Diptera. *Philosophical Transactions of the*
593 *Royal Society B: Biological Sciences*, *233*(602), 347–384.
594 https://www.jstor.org/stable/10.2307/j.ctt211qv60.7

595 Raad, H., Ferveur, J.-F., Ledger, N., Capovilla, M., & Robichon, A. (2016). Functional Gustatory Role of
596 Chemoreceptors in Drosophila Wings. *Cell Reports*, *15*(7), 1442–1454.
597 https://doi.org/10.1016/j.celrep.2016.04.040

598 Rajabi, H., & Gorb, S. N. (2020). How do dragonfly wings work? A brief guide to functional roles of wing
599 structural components. *International Journal of Odonatology*, *23*(1), 23–30.
600 https://doi.org/10.1080/13887890.2019.1677515

601 Rajabi, H., Moghadami, M., & Darvizeh, A. (2011). Investigation of microstructure, natural frequencies and
602 vibration modes of dragonfly wing. *Journal of Bionic Engineering*, *8*(2), 165–173.
603 https://doi.org/10.1016/S1672-6529(11)60014-0

604 Rajabi, H., Schroeter, V., Eshghi, S., & Gorb, S. N. (2017). The probability of wing damage in the dragonfly
605 Sympetrum vulgatum (Anisoptera: Libellulidae): a field study. *Biology Open*, *6*(9), 1290–1293.
606 https://doi.org/10.1242/bio.027078

607 Riek, E. F., & Kukalová-Peck, J. (1984). A new interpretation of dragonfly wing venation based upon Early Upper
608 Carboniferous fossils from Argentina (Insecta: Odonatoidea) and basic character states in pterygote
609 wings. *Canadian Journal of Zoology*, *62*(6), 1150–1166. https://doi.org/10.1139/z84-166

610 Ruppel, G. (1989). Kinematic Analysis of Symmetrical Flight Manoeuvres of Odonata. *Journal of Experimental*
611 *Biology*, *144*, 13–42.

612 Salcedo, M. K., & Socha, J. J. (2020). Circulation in Insect Wings. *Integrative and Comparative Biology*, *60*(5),
613 1208–1220. https://doi.org/10.1093/icb/icaa124

614 Schindelin, J., Arganda-Carreras, I., Frise, E., Kaynig, V., Longair, M., Pietzsch, T., Preibisch, S., Rueden, C.,
615 Saalfeld, S., Schmid, B., Tinevez, J.-Y., White, D. J., Hartenstein, V., Eliceiri, K., Tomancak, P., & Cardona,
616 A. (2012). Fiji: an open-source platform for biological-image analysis. *Nature Methods*, *9*(7), 676–682.
617 https://doi.org/10.1038/nmeth.2019

618 Selvakumar, R., Karuppanan, K. K., & Pezhinkattil, R. (2012). Analysis on surface nanostructures present in
619 hindwing of dragon fly (Sympetrum vulgatum) using atomic force microscopy. *Micron*, *43*(12), 1299–
620 1303. https://doi.org/10.1016/j.micron.2011.10.017

621 Shumway, N., Gabryszuk, M., & Laurence, S. (2020). The impact of dragonfly wing deformations on
622 aerodynamic performance during forward flight. *Bioinspiration & Biomimetics*, *15*(2), 026005.
623 https://doi.org/10.1088/1748-3190/ab597e

624 Simmons, P. (1977). The neuronal control of dragonfly flight. I. Anatomy. *Journal of Experimental Biology*, *71*,
625 123–140. https://doi.org/10.25911/5d7783acf1631

626 Simmons, P. (1977). The neuronal control of dragonfly flight. II. Physiology. *Journal of Experimental Biology*, *71*,
627 141–155.

628 Simmons, P. J. (1978). Crevice organs: Sensory structures on the wings of dragonflies (Insecta, Odonata).
629 *Zoomorphologie*, *89*(3), 251–255. https://doi.org/10.1007/BF00993951

630 Spinola, S. M., & Chapman, K. M. (1975). Proprioceptive indentation of the campaniform sensilla of cockroach
631 legs. *Journal of Comparative Physiology ? A*, *96*(3), 257–272. https://doi.org/10.1007/BF00612698

632 Sterbing-D'Angelo, S., Chadha, M., Chiu, C., Falk, B., Xian, W., Barcelo, J., Zook, J. M., & Moss, C. F. (2011). Bat
633 wing sensors support flight control. *Proceedings of the National Academy of Sciences*, *108*(27), 11291–
634 11296. https://doi.org/10.1073/pnas.1018740108

635 Sun, M. (2004). A computational study of the aerodynamic forces and power requirements of dragonfly
636 (Aeschna juncea) hovering. *Journal of Experimental Biology*, *207*(11), 1887–1901.
637 https://doi.org/10.1242/jeb.00969

638 Taylor, G. K., & Krapp, H. G. (2007). Sensory Systems and Flight Stability: What do Insects Measure and Why? In
639 *Advances in Insect Physiology* (Vol. 34, Issue 07, pp. 231–316). https://doi.org/10.1016/S0065-
640 2806(07)34005-8

641 Thomas, A. L. R. (2004). Dragonfly flight: free-flight and tethered flow visualizations reveal a diverse array of
642 unsteady lift-generating mechanisms, controlled primarily via angle of attack. *Journal of Experimental*
643 *Biology*, *207*(24), 4299–4323. https://doi.org/10.1242/jeb.01262

644 Vincent, J. F. V., Clift, S. E., & Menon, C. (2007). Biomimetics of campaniform sensilla: Measuring strain from
645 the deformation of holes. *Journal of Bionic Engineering*, *4*(2), 63–76. https://doi.org/10.1016/S1672-
646 6529(07)60015-8

647 Wakeling, J. M., & Ellington, C. P. (1997). Dragonfly flight II. Velocities, Accelerations and Kinematics of
648 Flapping Flight. *Journal of Experimental Biology*, *200*, 557–582.

649 Wang, J. K., & Sun, M. (2005). A computational study of the aerodynamics and forewing-hindwing interaction
650 of a model dragonfly in forward flight. *Journal of Experimental Biology*, *208*(19), 3785–3804.
651 https://doi.org/10.1242/jeb.01852

652 Wang, Z. J. (2004). The role of drag in insect hovering. *Journal of Experimental Biology*, *207*(23), 4147–4155.
653 https://doi.org/10.1242/jeb.01239

654 Wootton, R. (1992). Functional Morphology Of Insect Wings. *Annual Review of Entomology*, *37*(1), 113–140.
655 https://doi.org/10.1146/annurev.ento.37.1.113

656 Wootton, R. J. (1998). Smart Engineering in the Mid-Carboniferous: How Well Could Palaeozoic Dragonflies
657 Fly? *Science*, *282*(5389), 749–751. https://doi.org/10.1126/science.282.5389.749

658 Yarger, A. M., & Fox, J. L. (2018). Single mechanosensory neurons encode lateral displacements using precise
659 spike timing and thresholds. *Proceedings of the Royal Society B: Biological Sciences*, *285*(1887),
660 20181759. https://doi.org/10.1098/rspb.2018.1759

661 Yoshida, A., Noda, A., & Emoto, J. (2001). Bristle distribution along the wing margin of the small white cabbage
662 butterfly (Lepidoptera: Pieridae). *Annals of the Entomological Society of America*, *94*(3), 467–470.
663 https://doi.org/10.1603/0013-8746(2001)094[0467:BDATWM]2.0.CO;2

664 Zill, B. Y. S. N., & Moran, D. T. (1981). The Exoskeleton and Insect Proprioception. I. Responses of Tibial
665 Campaniform Sensilla to External and Muscle-Generated Forces in the American Cockroach, Periplaneta
666 Americana. *Journal of Experimental Biology*, *91*(1), 1–24.